

β -delayed one-neutron emission probabilities within a neural network modelDi Wu¹, C. L. Bai¹, H. Sagawa^{2,3}, S. Nishimura², and H. Q. Zhang⁴¹*College of Physics, Sichuan University, Chengdu 610065, China*²*RIKEN Nishina Center, Wako 351-0198, Japan*³*Center for Mathematics and Physics, University of Aizu, Aizu-Wakamatsu, Fukushima 965-8560, Japan*⁴*China Institute of Atomic Energy, Beijing 102413, China*

(Received 22 March 2021; revised 31 August 2021; accepted 27 October 2021; published 8 November 2021)

β -delayed neutron emission is one of the key ingredients for astrophysical r -process nucleosynthesis, and theoretical model predictions have still large uncertainties. In this work, we apply a novel feed-forward neural network model to calculate accurately β -delayed one-neutron emission probabilities. A model is trained with a set of input data of known physical quantities; one-neutron emission Q value, the Q -value difference between the one- and two-neutron emissions, β -decay half-life, the distance from the least neutron-rich nucleus with $Q_{\beta 1n} > 0$ in each isotope, and the exponential form of the ratio of Q -value $\exp(-Q_{\beta 2n}/Q_{\beta 1n})$. The results give improvements for predictions of medium heavy isotopes and provide reasonable results in r -process nuclei, especially in the waiting point nuclei for neutron magic numbers $N = 50$ and 82 , in comparison with other microscopic models.

DOI: [10.1103/PhysRevC.104.054303](https://doi.org/10.1103/PhysRevC.104.054303)**I. INTRODUCTION**

Much attention has been paid recently to the study of β -delayed neutron emission, which occurs when the Q value of β decay for parent nucleus (AZ) is larger than the one-neutron separation energy of its daughter nucleus. This process has a strong impact on various physical problems such as nuclear structure, nuclear astrophysics, and reactor physics. The neutron emission probability P_n is an important ingredient for r -process nucleosynthesis modeling [1–4]; i.e., they indicate the detours of the r -process paths back to the stability line and provide also additional neutrons for the late stage of neutron recapture.

Starting from the pioneering work of Roberts *et al.* [5,6], considerable efforts have been devoted to the precise experimental measurements of P_n . As of August 2020, β -delayed one-neutron branching ratios (P_{1n}) were measured in 306 nuclei with $2 \leq Z \leq 57$, β -delayed two-neutron branching ratios (P_{2n}) were measured in 31 nuclei, and β -delayed three-neutron branching ratios (P_{3n}) were measured in 4 nuclei. The compilation of experimental P_n measurements can be found in Refs. [7–9] and references therein. Very recently, the P_{1n} s for r -process nuclei around $N = 82$ are measured in RIKEN [10]. In this work, we concentrate on the prediction of P_{1n} values, since most of the new data in the experimental Terra Incognita on the neutron-rich side will involve β -delayed neutron emitters. Furthermore, many key P_{1n} data of neutron-rich nuclei for r -process nucleosynthesis are still not measured or out of experimental reach.

Theoretically, the precise prediction for P_{1n} is a great challenge due to the sensitivity of the neutron emission on the energies and strengths of the low-lying β spectrum of the

parent nucleus (AZ) and the competition mechanisms between one-neutron and other decay processes [11], which are difficult to take into account in theoretical calculations. There are two groups of models for β -delayed neutron emissions, i.e., semiempirical and microscopic ones. The microscopic models are the proton-neutron quasiparticle random phase approximation (pn -QRPA) [12–17], and shell model [18–20]. These models adopt either phenomenological or realistic nucleon-nucleon interactions and take the allowed Gamow-Teller and first-forbidden decays into consideration. There are also some semiempirical models for the systematic calculations of the P_{1n} , such as Amiel's expression [21], the Kratz-Herrmann formula (KHF) [22], the improved KHF [23], and Miernik's model [24]. The semiempirical models describe the correlations between the P_{1n} and other β -decay gross properties such as β -decay half-lives $T_{1/2}$, Q values, and one-neutron separation energy S_n .

Recently, the machine learning (ML) technique, based on the neural networks, has been frequently used in physics of complex systems, due to its powerful and convenient inference abilities. There are many successful examples of the applications of neural networks in nuclear physics, such as the predictions of nuclear charge radii [25–28], nuclear mass [29–32], the β -decay half-lives [33], dripline locations [34,35], the fission product yields [36,37], the isotopic cross sections in proton-induced spallation reactions [38,39], the ground-state and excited energies [40,41], the nuclear liquid-gas phase transition [42], and the nuclear energy density functionals [43]. In our previous work [25], the fully connected feed-forward neural network (FNN) was applied to study the nuclear charge radii. The FNN is a standard model of ML, which can be viewed as a nonlinear function to construct

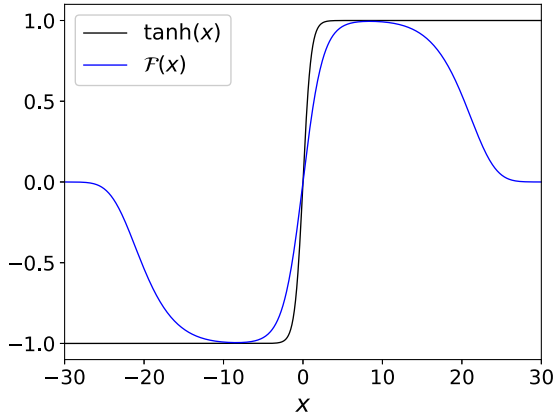


FIG. 1. Shape of the activation functions, $\tanh(x)$ and $\mathcal{F}(x)$. $\mathcal{F}(x) = 2(1 - \frac{1}{1 + \exp(-(ax)^b)})\tanh(cx)$; the values a , b , and c are taken as 0.05, 6, and 0.4, respectively. See the text for details.

the input-output mapping for a given data set. In this work, the FNN model is applied to calculate and predict the P_{1n} .

This paper is organized as follows. In Sec. II, we give a brief introduction of the FNN model. The data preprocessing is introduced in Sec. III. The predicting results of P_{1n} as well as the discussion are presented in Sec. IV. Finally in Sec. V, we give the summary of our work.

II. FNN MODEL

In this work, we take a three-layer FNN architecture, which consists of input, hidden, and output layers. The corresponding numbers of neurons in these three layers are N_{in} , N_h , and N_o , respectively. The number of the network parameters is $\sum_{i=1}^2 N_i \times N_{i+1}$, where N_i is the number of neurons in the i th layer. More details on the FNN model can be found in Refs. [25,41].

In our present research, a new activation function $\mathcal{F}(x)$ is introduced in the hidden layer rather than the widely applied function, $\tanh(x)$. The function $\mathcal{F}(x)$ is defined as

$$\mathcal{F}(x) = 2\left(1 - \frac{1}{1 + \exp(-(ax)^b)}\right)\tanh(cx), \quad (1)$$

where a , c are real numbers and b is a positive even integer. Among them, a and b collaborate to dominate the saturation and damping regions of $\mathcal{F}(x)$, and c controls the linear region of $\mathcal{F}(x)$. In the calculations, a , b , and c are optimized to be 0.05, 6, and 0.4, respectively. The shapes of $\mathcal{F}(x)$ and $\tanh(x)$ are shown in Fig. 1. The corresponding linear, saturation, and damping regions are $|x| \in (0, 5)$, $(5, 10)$, and $(10, 25)$, respectively. In comparison with $\tanh(x)$, $\mathcal{F}(x)$ has extra damping regions for $|x| \in (10, 25)$. Thus, $\mathcal{F}(x)$ vanishes for large absolute x value. The linear region of $\mathcal{F}(x)$ is larger than that of $\tanh(x)$. With these properties, $\mathcal{F}(x)$ can acquire more information and drop the abnormal outputs.

For the output layer, the sigmoid function is adopted as the activation function

$$\text{sigmoid}(x) = \frac{1}{1 + e^{-x}}, \quad (2)$$

which ranges from 0 to 1 for $x \in [-\infty, +\infty]$. In order to describe well the P_{1n} , we take the loss function as

$$\text{Loss}(\mathbf{P}_{1n}(\text{th.}), \mathbf{P}_{1n}(\text{exp.})) = \frac{1}{N} \sum_{i=1}^N \left[100[P_{1n}^i(\text{th.}) - P_{1n}^i(\text{exp.})]^2 + \frac{P_{1n}^i(\text{th.})}{P_{1n}^i(\text{exp.})} \right], \quad (3)$$

where N is the number of data in the training set. The first term in the loss function is the mean squared error (MSE), which quantifies the deviation between the theoretical values and the experimental data. The weight 100 in this term intends to make the two terms equal in the order of magnitude. Namely, since the $0 \leq P_{1n} \leq 1$, the deviation $[P_{1n}(\text{th.}) - P_{1n}(\text{exp.})]^2$ is in the order of 10^{-2} for most nuclei, while the second term is in the order of 10^0 for most nuclei if the network is well trained. The second term is to make sure whether the model gives a good description of P_{1n} depending on its value.

The learning process is performed to minimize the loss function via proper optimization methods. We use the root mean squared Prop (RMSProp) method [44] to obtain the optimal network parameters. The RMSProp is a popular alternative to the stochastic gradient descent (SGD) method [45], which is one of the most widely used training algorithms.

To reduce the overfitting, the dropout algorithm is adopted in the training and testing processes. The dropout algorithm is a newly developed approach, which has achieved a satisfactory performance in alleviating the overfitting of the neural network. In the training procedure, the neuron in the hidden layer is activated by a probability p . To be more specific, the neuron is called nonactivated if its output is discarded (i.e., set to zero); otherwise it is activated. In the present dropout approach, the discard probability p is set to the value 0.5, which is a default value in the algorithm. In the testing procedure, where the dropout algorithm is also adopted, we calculate the P_{1n} values with the trained models for 1000 times individually, and the average value is taken as the final result of the given model.

The network contains hundreds of parameters so that the output of the final optimized model is very much related to the initialization of the model at the beginning of the training approach. Thus, we repeat the training approach 50 times; i.e., we train 50 different models and each model corresponds to a certain parameter initialization. Finally, the mean value of the outputs of these 50 models is taken as the FNN result.

III. DATA PREPROCESSING

In machine learning, the inputs of the network should be prepared in a form either reflecting the relevance to the output data or convenient for the network to grasp the specific features of the input data. In the theoretical models, the P_{1n} value is related to the Q value of one- and two-neutron emissions $Q_{\beta 1n}$ and $Q_{\beta 2n}$, and the β -decay half-life $T_{1/2}$. In addition, we noticed that the P_{1n} will suddenly become large compared with its neighbor nuclei if there is a shell closure of neutrons in the daughter nuclei. This indicates that the neutron magic numbers produce a strong effect on the P_{1n} . Thus, the two-neutron separation energy difference between nuclei $^{A+1}Z + 1$

and $A^{-1}Z + 1$, $\Delta S_{2n} = S_{2n}(Z + 1, N) - S_{2n}(Z + 1, N - 2)$ is taken into consideration as an indicator of the shell closures.

The above raw data are arranged to be the inputs of the network: The inputs for the network training are $Q_{\beta 1n}$, $(\Delta E_w)^d T_{1/2}$, a function $\mathcal{G}(Z, N)$, and the distance from the least neutron-rich nucleus with $Q_{\beta 1n} > 0$ for each isotope $N - N_D$, where N_D is the neutron number of the least neutron-rich nucleus with $Q_{\beta 1n} > 0$ for each isotope. In the above, the ΔE_w is the Q -value difference between one- and two-neutron emissions $\Delta E_w = Q_{\beta 1n} - Q_{\beta 2n}$. For the nuclei with only one-neutron emission, the ΔE_w equals to $Q_{\beta 1n}$. The power d on ΔE_w is optimized to be 3.0, varying in a range between 2.0 to 5.0 to produce reasonable results of the testing data set. This input is similar to that proposed in the improved KHF model in Ref. [23].

In the present calculations, the Q values of one- and two-neutron emissions are taken from Refs. [7,8], and the binding energies are taken from Ref. [46,47]. The function $\mathcal{G}(Z, N)$ is defined as

$$\mathcal{G}(Z, N) = \Delta E_w \Delta S_{2n}, \quad (4)$$

where the information of Q -value difference ΔE_w and the neutron magic number of daughter nuclei are involved.

Since there are competitions between the one-neutron emission and other neutron emission processes, we first calculate P_{1n} of the nuclei with only one-neutron emission in Sec. IV A. Then the model is extended to calculate P_{1n} for the nuclei with and without multineutron emission in Sec. IV B, taking into account the exponential form of the ratio of the Q -value $\exp(-Q_{\beta 2n}/Q_{\beta 1n})$ as an extra input.

The data set of the present ML-FNN model is divided into two parts, i.e., the training set and the testing set, which are selected randomly 1000 times. After the root mean squared deviations (RMSD) between theoretical and experimental results were obtained, the data set with the minimum RMSD difference between the training set and the testing set is chosen for the final results. In all of the selections, the size of training set is about 70% of the total data set, which is the usual choice, in order to get the network as accurate as possible and test its predicting ability.

IV. RESULTS AND DISCUSSION

The FNN model is applied to study the P_{1n} of light and medium heavy nuclei with $2 < Z < 57$. In this section, we discuss first the nuclei in which only one-neutron emission take place (Sec. IV A), and then the P_{1n} of the nuclei which both the one-neutron and the multineutron emission take place are also studied (Sec. IV B).

A. P_{1n} for nuclei with only one-neutron emission

In this section, we calculate the P_{1n} of the nuclei with only one-neutron emission. There are 127 nuclei in the input data, and the size of the training set is 89, as shown in Fig. 2(a). In the network, the inputs are $Q_{\beta 1n}$, $\Delta E_w^3 T_{1/2}$, $\mathcal{G}(Z, N)$, and $N - N_D$, in which ΔE_w is actually $Q_{\beta 1n}$ in this special case. The numbers of neurons in the input, hidden, and output layers are 4, 40, and 1, respectively. Thus, the corresponding

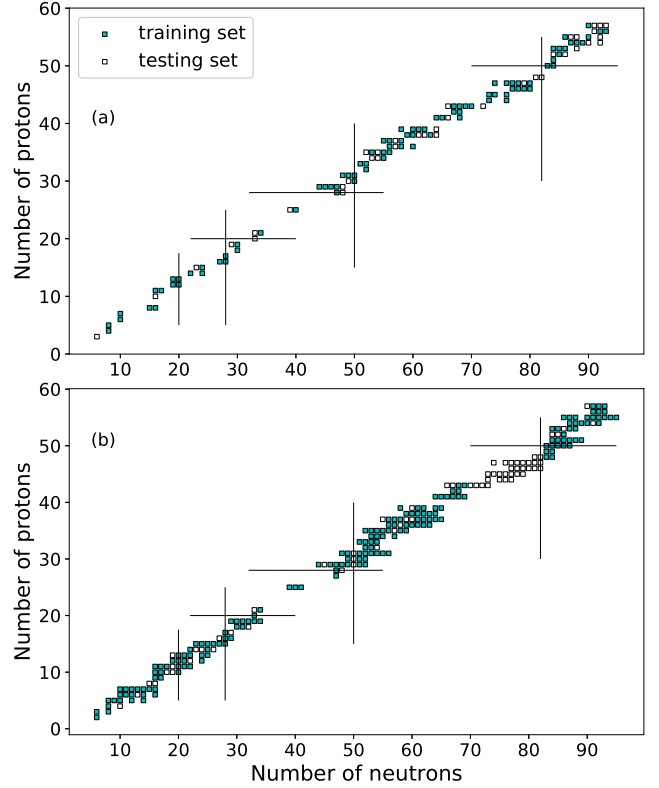


FIG. 2. The nuclei for training set (cyan squares) and the testing set (white squares). The upper panel shows the nuclei with only one-neutron emission, while the lower panel shows the nuclei both with and without multineutron emission. See the text for details.

number of network parameters is 200. The P_{1n} differences between the present ML-FNN and experimental data of these nuclei are shown in Fig. 3, together with the ones obtained by the FRDM12 + (Q)RPA + HF [17] and RHB + RQRPA [16]. As is shown in the figure, the results of the three models show reasonable agreement with the experimental data. The differences between the ML-FNN and experimental data are distributed in a range from -25% to 25% and quite concentrated around 0 especially when $N > 40$. The RMSD of ML-FNN are 8.5% for training set and 9.0% for testing set, while it is 11.8% and 13.4% for the FRDM12 + (Q)RPA + HF and RHB + RQRPA models, respectively. There is a remarkable improvement of ML-FNN model in the RMSD in comparisons with the other two models.

B. P_{1n} for nuclei both with and without multineutron emission

The multineutron emission process will become more dominant in more neutron-rich nuclei. In order to extend the ML-FNN model to these nuclei, the exponential form of the ratio of Q -value $\exp(-Q_{\beta 2n}/Q_{\beta 1n})$ is introduced in the present model. There are 244 nuclei in the data set, in which 178 nuclei are taken as the training set, as shown in Fig. 2(b). To check the predicting power of the model, the 28 r -process nuclei newly measured in RIKEN [10] are put in the testing set. Furthermore, the 6 waiting-point nuclei with magic numbers

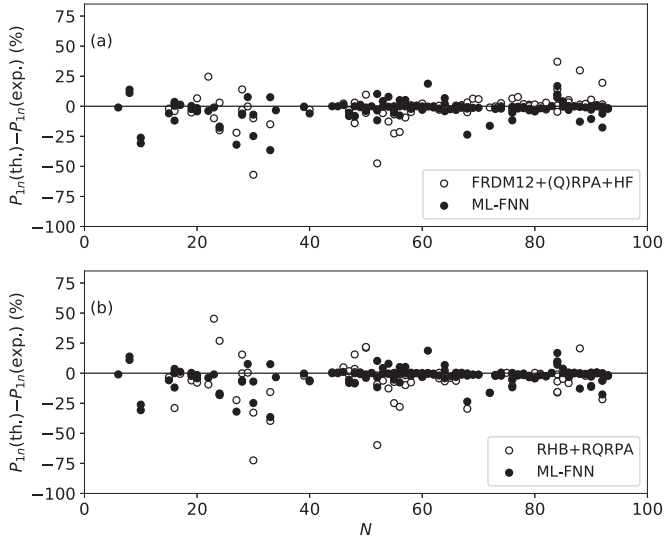


FIG. 3. Differences of P_{1n} between theoretical results and the experimental data for the nuclei with only one-neutron emission. The data of FRDM12 + (Q)RPA + HF are taken from Ref. [17], and the data of RHB + RQRPA are taken from Ref. [16]. See the text for details.

$N = 50$ and 82 are also put in the testing set. The other 32 nuclei in the testing set are chosen randomly. The numbers of neurons in the input, hidden, and output layers are 5, 60, and 1, respectively. The corresponding number of network parameters is 360.

The P_{1n} differences between the theoretical results and the experimental data are shown for the neutron numbers $8 \leq N \leq 95$ in Fig. 4. The results of ML-FNN and the FRDM12 + (Q)RPA + HF model are shown in Fig. 4(a), while the results of ML-FNN and RHB + RQRPA model are shown in Fig. 4(b). The FRDM12 + (Q)RPA + HF model is successful in the region $40 < N < 80$, especially in the region $60 < N <$

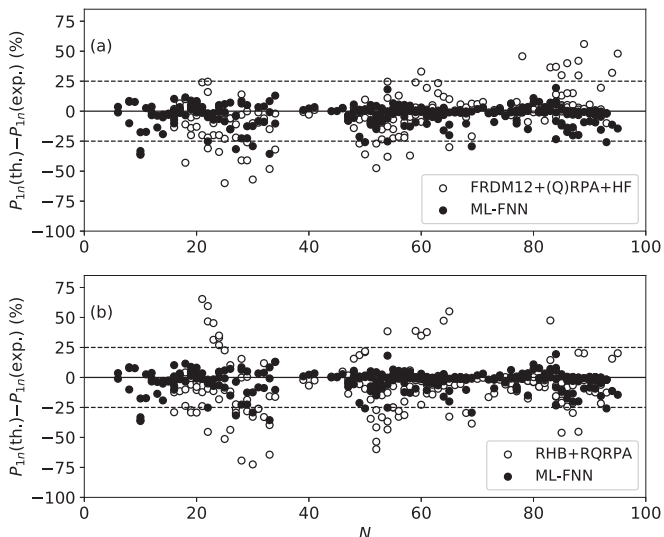


FIG. 4. The same as Fig. 3, but for the nuclei with and without the multineutron emission. See the text for details.

80 which attained the highest accuracy, but it underestimates and overestimates the P_{1n} values in the $N < 40$ and $N > 80$ regions, respectively. The FRDM12 + (Q)RPA + HF model provides the P_{1n} values with differences from the experimental data, varying from about -60% in lighter mass nuclei to about 50% in heavy nuclei $N > 80$. The results of RHB + RQRPA model underestimates the P_{1n} for many nuclei and also overestimates for nuclei with $N \approx 25$ and $N \approx 65$. For the nuclei with $N > 70$, RHB + RQRPA model gives a better description compared with the lighter nuclei with $N < 70$. Most of the differences of P_{1n} between the RHB + RQRPA results and the experimental data vary from about -40% to 25% in the region with $N > 70$. The present ML-FNN model provides reasonable results in the whole region with differences varying from about -25% to 25% , showing a more narrower distribution around the zero value in Fig. 4.

We analyze the RMSD of the theoretical models in comparisons with the experimental data. The RMSD values of ML-FNN model together with the FRDM12 + (Q)RPA + HF [17] and RHB + RQRPA [16] are listed in Table I. For the ML-FNN model, RMSD values of the training set, the testing set, as well as the total data set (ML-FNN_{tot.}) are shown. A small difference of RMSD, 0.3% , between the training set and testing set indicates the reasonable predicting power of the present ML-FNN model. For the total data set, the ML-FNN model gives the lowest RMSD value among the three theoretical models. Compared with the RMSD for nuclei with the only one-neutron emission (see Sec. IV A), the RMSD of the nuclei both with and without multineutron emission is slightly increased by about 1% in the ML-FNN. It should be noticed that the competition between one- and two-neutron emission is only considered in the present ML-FNN model. On top of that, the γ -decay process is also compete with these neutron emissions. The latter process remains for a future study.

In the nucleosynthesis, the r -process is one of the major processes for the formations of heavy elements. Recently, the P_{1n} for r -process nuclei around $N = 82$ are measured in RIKEN [10]. These experimental results are shown in Fig. 5 together with the results of different theoretical models, i.e., ML-FNN, FRDM12 + (Q)RPA + HF, and the RHB + RQRPA models. In the figure, the experimental data of P_{1n} for $^{109-114}_{43}\text{Tc}$ are taken from Ref. [8], while the others are taken from Ref. [10], which are put in the testing set. As already shown in Fig. 4, the FRDM12 + (Q)RPA + HF has a remarkable accuracy in these r -process nuclei. Figure 5 shows that the ML-FNN and FRDM12 + (Q)RPA + HF models are equally precise in predicting the P_{1n} values for these r -process nuclei. Except for $^{109,110}_{43}\text{Tc}$ and $^{116}_{44}\text{Ru}$, the results of RHB + RQRPA model underestimates the experimental values of these isotopes.

The waiting-point nuclei are the key elements to determine the timescale of r -process, and strongly affect the final abundance of elements in the solar system. The experimental P_{1n} values of the waiting-point nuclei given in Refs. [20,48,49] at the magic neutron numbers $N = 50, 82$ are listed together with theoretical ones in Table II. For the $N = 50$ isotones, the experimental data show a drop at $Z = 30$. The FRDM12 + (Q)RPA + HF model failed to reproduce this trend, while both the ML-FNN model and RHB + RQRPA reproduce this

TABLE I. RMSD of P_{1n} of the nuclei both with and without multineutron emission for ML-FNN, FRDM12+(Q)RPA+HF [17], and RHB+RQRPA [16] models. The values are given in unit of %.

	ML-FNN	ML-FNN _{tot.}	FRDM12+(Q)RPA+HF	RHB+RQRPA
Training set	9.7	9.8	17.4	20.9
Testing set	10.0			

drop successfully. The ML-FNN model reproduces the results most accurately among the three theoretical models for the $N = 50$ isotones. For the $N = 82$ isotones, the experimental data show a peak at $Z = 47$. All of the three theoretical models reproduce this trend successfully. Quantitatively, except for $^{128}_{46}\text{Pd}_{82}$, the results of ML-FNN are at the highest accuracy among the three theoretical models. Thus, the present ML-FNN model provides P_{1n} values of the waiting-point nuclei at $N = 50$ and 82 with the highest accuracy qualitatively and quantitatively.

V. SUMMARY

In summary, the ML-FNN model was applied to study the β -delayed one-neutron emission in light and medium heavy nuclei in a wide region of nuclei with $2 \leq Z \leq 57$. In the present ML-FNN model, the new activation function $\mathcal{F}(x)$ has been introduced to the hidden layer, which can acquire more information and drops the abnormal outputs. In the training, the network takes into account in the inputs, the Q values of one- and two-neutron emissions, the half-life $T_{1/2}$,

the shell closure information of daughter nuclei implemented by the two-neutron separation energy ΔS_{2n} , and the distance from the least neutron-rich nucleus with $Q_{\beta 1n} > 0$ for each isotope.

For the nuclei both with and without multineutron emissions, the RMSD of the P_{1n} values between the theoretical and experimental results is about 9.8% in the present model, while those for RHB + QRPA and FRDM12 + (Q)RPA + HF are about 20.9% and 17.4%, respectively. For the latest measured r -process nuclei, the present ML-FNN model provides the fine results similar to the FRDM12 + (Q)RPA + HF model, which attains its highest accuracy in this region, as shown in Fig. 4. Furthermore, for the waiting point nuclei at $N = 50$ and 82 magic numbers, the ML-FNN model produces P_{1n} values with the highest accuracy qualitatively and quantitatively. The performance of the FNN model in the present study indicates that it may provide reliable predictions of unknown P_{1n} values for unstable nuclei along the paths of r -process nucleosynthesis and open new opportunities for the study of astrophysical process with unstable nuclei. The research in this direction is in progress.

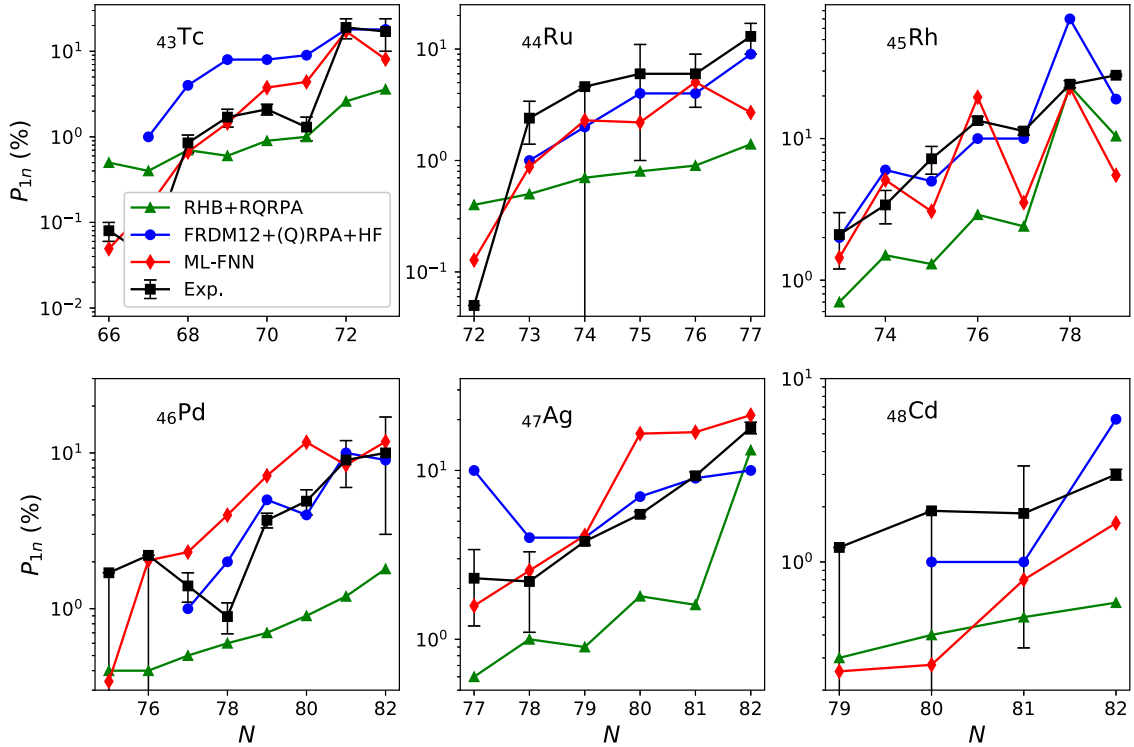


FIG. 5. Comparisons of P_{1n} for the r -process nuclei around $N = 82$ between the experimental data (black squares) [8,10] and the theoretical results. The experimental data of $^{109-114}_{43}\text{Tc}$ are taken from Ref. [8], while the others are taken from Ref. [10]. Three different theoretical models are ML-FNN (red diamonds), FRDM12 + (Q)RPA + HF (blue circles) [12], and RHB + RQRPA (green triangles) [16]. See the text for details.

TABLE II. The P_{1n} of the waiting-point nuclei at the magic neutron numbers $N = 50$ and 82 . Three theoretical models (FRDM12+(Q)RPA+HF [17], RHB+RQRPA [16], and ML-FNN) and the experimental data [8,10] are listed. The values are given in unit of %.

Nuclides	FRDM12+(Q)RPA+HF	RHB+RQRPA	ML-FNN	Exp.
$^{79}_{29}\text{Cu}_{50}$	30.0	56.5	40.1	66(12)
$^{80}_{30}\text{Zn}_{50}$	11.0	22.5	1.6	1.36(12)
$^{81}_{31}\text{Ga}_{50}$	7.0	34.3	14.1	12.5(8)
$^{128}_{46}\text{Pd}_{82}$	9.0	1.8	11.8	10(7)
$^{129}_{47}\text{Ag}_{82}$	10.0	13.2	21.2	17.9(14)
$^{130}_{48}\text{Cd}_{82}$	6.0	0.7	1.6	3.0(2)

ACKNOWLEDGMENTS

This work is supported by the National Natural Science Foundation of China under Grants No. 11575120 and No. 11822504 and Science Specialty Program of Sichuan

University under Grant No. 2020SCUNL210. This work is also supported by JSPS KAKENHI (Grants No. JP19K03858, No. JP19K03858, No. 17H06090, and No. 20H05648) and the RIKEN program for Evolution of Matter in the Universe (r-EMU).

- [1] A. Arcones and G. Martínez-Pinedo, *Phys. Rev. C* **83**, 045809 (2011).
- [2] M. Mumpower, R. Surman, G. McLaughlin, and A. Aprahamian, *Prog. Part. Nucl. Phys.* **86**, 86 (2016).
- [3] C. J. Horowitz, A. Arcones, B. Côté, I. Dillmann, W. Nazarewicz, I. U. Roederer, H. Schatz, A. Aprahamian, D. Atanasov, A. Bauswein, T. C. Beers, J. Bliss, M. Brodeur, J. A. Clark, A. Frebel, F. Foucart, C. J. Hansen, O. Just, A. Kankainen, G. C. McLaughlin *et al.*, *J. Phys. G: Nucl. Part. Phys.* **46**, 083001 (2019).
- [4] J. J. Cowan, C. Sneden, J. E. Lawler, A. Aprahamian, M. Wiescher, K. Langanke, G. Martínez-Pinedo, and F.-K. Thielemann, *Rev. Mod. Phys.* **93**, 015002 (2021).
- [5] R. B. Roberts, R. C. Meyer, and P. Wang, *Phys. Rev.* **55**, 510 (1939).
- [6] R. B. Roberts, L. R. Hafstad, R. C. Meyer, and P. Wang, *Phys. Rev.* **55**, 664 (1939).
- [7] M. Birch, B. Singh, I. Dillmann, D. Abriola, T. D. Johnson, E. A. McCutchan, and A. A. Sonzogni, *Nucl. Data Sheets* **128**, 131 (2015).
- [8] J. Liang, B. Singh, E. A. McCutchan, I. Dillmann, M. Birch, A. A. Sonzogni, X. Huang, M. Kang, J. Wang, G. Mukherjee, K. Banerjee, D. Abriola, A. Algora, A. A. Chen, T. D. Johnson, and K. Miernik, *Nucl. Data Sheets* **168**, 1 (2020).
- [9] P. Dimitriou, I. Dillmann, B. Singh, V. Piksaikin, K. P. Rykaczewski, J. L. Tain, A. Algora, K. Banerjee, I. N. Borzov, D. Cano-Ott, S. Chiba, M. Fallot, D. Foligno, R. Grzywacz, X. Huang, T. Marketin, F. Minato, G. Mukherjee, B. C. Rasco, A. Sonzogni *et al.*, *Nucl. Data Sheets* **173**, 144 (2021).
- [10] O. Hall, T. Davinson, A. Estrade, J. Liu, G. Lorusso, F. Montes, S. Nishimura, V. H. Phong, P. J. Woods, J. Agramunt, D. S. Ahn, A. Algora, J. M. Allmond, H. Baba, S. Bae, N. T. Brewer, C. G. Bruno, R. Caballero-Folch, F. Calviño, P. J. Coleman-Smith *et al.*, *Phys. Lett. B* **816**, 136266 (2021).
- [11] M. R. Mumpower, T. Kawano, and P. Möller, *Phys. Rev. C* **94**, 064317 (2016).
- [12] P. Möller, B. Pfeiffer, and K.-L. Kratz, *Phys. Rev. C* **67**, 055802 (2003).
- [13] F. Minato and O. Iwamoto, *Prog. Nucl. Energy* **82**, 112 (2015).
- [14] D. L. Fang, B. A. Brown, and T. Suzuki, *Phys. Rev. C* **88**, 024314 (2013).
- [15] D. L. Fang, B. A. Brown, and T. Suzuki, *Phys. Rev. C* **88**, 034304 (2013).
- [16] T. Marketin, L. Huther, and G. Martínez-Pinedo, *Phys. Rev. C* **93**, 025805 (2016).
- [17] P. Möller, M. Mumpower, T. Kawano, and W. Myers, *At. Data Nucl. Data Tables* **125**, 1 (2019).
- [18] S. Yoshida, Y. Utsuno, N. Shimizu, and T. Otsuka, *Phys. Rev. C* **97**, 054321 (2018).
- [19] G. Martínez-Pinedo and K. Langanke, *Phys. Rev. Lett.* **83**, 4502 (1999).
- [20] Q. Zhi, E. Caurier, J. J. Cuenca-García, K. Langanke, G. Martínez-Pinedo, and K. Sieja, *Phys. Rev. C* **87**, 025803 (2013).
- [21] S. Amiel and H. Feldstein, *Phys. Lett. B* **31**, 59 (1970).
- [22] K.-L. Kratz and G. Herrmann, *Z. Phys. A* **263**, 435 (1972).
- [23] E. A. McCutchan, A. A. Sonzogni, T. D. Johnson, D. Abriola, M. Birch, and B. Singh, *Phys. Rev. C* **86**, 041305(R) (2012).
- [24] K. Miernik, *Phys. Rev. C* **88**, 041301(R) (2013).
- [25] D. Wu, C. L. Bai, H. Sagawa, and H. Q. Zhang, *Phys. Rev. C* **102**, 054323 (2020).
- [26] Y. F. Ma, C. Su, J. Liu, Z. Z. Ren, C. Xu, and Y. H. Gao, *Phys. Rev. C* **101**, 014304 (2020).
- [27] R. Utama, W.-C. Chen, and J. Piekarewicz, *J. Phys. G* **43**, 114002 (2016).
- [28] S. Akkoyun, T. Bayram, S. O. Kara, and A. Sinan, *J. Phys. G: Nucl. Part. Phys.* **40**, 055106 (2013).
- [29] R. Utama, J. Piekarewicz, and H. B. Prosper, *Phys. Rev. C* **93**, 014311 (2016).
- [30] Z. M. Niu and H. Z. Liang, *Phys. Lett. B* **778**, 48 (2018).
- [31] X. H. Wu and P. W. Zhao, *Phys. Rev. C* **101**, 051301(R) (2020).
- [32] Y. F. Liu, C. Su, J. Liu, P. Danielewicz, C. Xu, and Z. Z. Ren, *Phys. Rev. C* **104**, 014315 (2021).
- [33] Z. M. Niu, H. Z. Liang, B. H. Sun, W. H. Long, and Y. F. Niu, *Phys. Rev. C* **99**, 064307 (2019).
- [34] L. Neufcourt, Y. Cao, W. Nazarewicz, and F. Viens, *Phys. Rev. C* **98**, 034318 (2018).

- [35] L. Neufcourt, Y. Cao, W. Nazarewicz, E. Olsen, and F. Viens, *Phys. Rev. Lett.* **122**, 062502 (2019).
- [36] Z. A. Wang, J. C. Pei, Y. Liu, and Y. Qiang, *Phys. Rev. Lett.* **123**, 122501 (2019).
- [37] C. Y. Qiao, J. C. Pei, Z. A. Wang, Y. Qiang, Y. J. Chen, N. C. Shu, and Z. G. Ge, *Phys. Rev. C* **103**, 034621 (2021).
- [38] C. W. Ma, D. Peng, H. L. Wei, Z. M. Niu, Y. T. Wang, and R. Wada, *Chin. Phys. C* **44**, 014104 (2020).
- [39] C. W. Ma, D. Peng, H. L. Wei, Y. T. Wang, and J. Pu, *Chin. Phys. C* **44**, 124107 (2020).
- [40] R. D. Lasserri, D. Regnier, J. P. Ebran, and A. Penon, *Phys. Rev. Lett.* **124**, 162502 (2020).
- [41] G. A. Negoita, G. R. Luecke, J. P. Vary, P. Maris, A. M. Shirokov, I. J. Shin, Y. Kim, E. G. Ng, and C. Yang, [arXiv:1803.03215v1](https://arxiv.org/abs/1803.03215v1).
- [42] R. Wang, Y. G. Ma, R. Wada, L.-W. Chen, W. B. He, H. L. Liu, and K. J. Sun, *Phys. Rev. Research* **2**, 043202 (2020).
- [43] X. H. Wu, Z. X. Ren, and P. W. Zhao, [arXiv:2105.07696](https://arxiv.org/abs/2105.07696).
- [44] T. Tieleman and G. Hinton, *Coursera Neural Netw. Mach. Learn.* **4**, 26 (2012).
- [45] L. Bottou, *Proceedings of Neuro-Nimes* **91**, 12 (1991).
- [46] W. J. Huang, M. Wang, F. G. Kondev, G. Audi, and S. Naimi, *Chin. Phys. C* **45**, 030002 (2021).
- [47] M. Wang, W. J. Huang, F. G. Kondev, G. Audi, and S. Naimi, *Chin. Phys. C* **45**, 030003 (2021).
- [48] J. Engel, M. Bender, J. Dobaczewski, W. Nazarewicz, and R. Surman, *Phys. Rev. C* **60**, 014302 (1999).
- [49] D. D. Ni and Z. Z. Ren, *J. Phys. G: Nucl. Part. Phys.* **41**, 025107 (2014).